How to cite: Angew. Chem. Int. Ed. **2022,** *61,* e202202098
International Edition: doi.org/10.1002/anie.202202098
German Edition: doi.org/10.1002/ange.202202098

Iridium Photocatalysts

Single-Cell Quantification of a Highly Biocompatible Dinuclear Iridium(III) Complex for Photocatalytic Cancer Therapy

Zhongxian Fan, Yi Rong, Tumpa Sadhukhan, Shaoxia Liang, Wenqing Li, Zhanxiang Yuan, Zilin Zhu, Shunwen Guo, Shaomin Ji, Jinquan Wang, Rajesh Kushwaha, Samya Banerjee, Krishnan Raghavachari, and Huaiyi Huang**

Abstract: Quantifying the content of metal-based anticancer drugs within single cancer cells remains a challenge. Here, we used single-cell inductively coupled plasma mass spectrometry to study the uptake and retention of mononuclear (**Ir1**) and dinuclear (**Ir2**) Ir^{III} photoredox catalysts. This method allowed rapid and precise quantification of the drug in individual cancer cells. Importantly, **Ir2** showed a significant synergism but not an additive effect for NAD(P)H photocatalytic oxidation. The lysosome-targeting **Ir2** showed low dark toxicity in vitro and *in vivo*. **Ir2** exhibited high photocatalytic therapeutic efficiency at 525 nm with an excellent photo-index in vitro and in tumor-bearing mice model. Interestingly, the photocatalytic anticancer profile of the dinuclear **Ir2** was much better than the mononuclear **Ir1**, indicating for the first time that dinuclear metal-based photocatalysts can be applied for photocatalytic anticancer treatment.

Introduction

As a leading cause of death worldwide, cancer is a major barrier to improving the health and quality of human life.[1] Recently, as one of the tools to address this challenge, the concept of photocatalytic cancer drugs was introduced.[2] The main advantages of this new concept are 1) significant spatiotemporal control over the drug activation that is helpful to overcome the drug resistance problem of Pt-based cancer drugs; 2) its anticancer effect with a very low concentration of metal complexes.[3] In this context, Ir^{III} complexes are emerging as promising candidates for photocatalytic cancer therapy due to their tunable structure and redox potential, significant photostability, notably high excited-state lifetimes, and multiple photosensitization mechanisms.[4] It is important to mention that in recent years, several Ir^{III}-based photosensitizers have been also developed for photoactivated cancer therapy.[5–14] These photosensitizers showed photo-triggered anticancer activity mainly via intracellular generation of reactive oxygen species (ROS).[5–14] Interestingly, Ir^{III}-based complexes have also been reported for cancer diagnosis and imaging.[15] For example, Ma and co-workers have developed an Ir^{III} complex to visualize β-galactosidase, the crucial biomarker for ovarian cancers.[15a] Moreover, organo-Ir^{III} complexes are reported to induce cancer cell death even under hypoxia via the photo-oxidation of cellular coenzyme, the reduced nicotinamide adenine dinucleotide (NADH) and reduction of cytochrome $C_{Fe(III)}$.[16] Such hypoxic tumors are known to be one of the main problems for cancer treatment.[17] It is important to mention that though there have been a few reports of photocatalytic cancer drug development based on mononuclear Ir^{III} complexes, the development of dinuclear Ir^{III}-based photocatalytic cancer drugs has not been explored so far and still remains a big challenge.[6,18]

In the development of cancer drugs, the uptake and retention of cancer drugs in every cancer cell are two highly important parameters.[19] One of the main causes of cisplatin resistance is the low retention of cisplatin in cancer cells.[20] Thus, quantification of the intracellular uptake of metal-

---

[*] Z. Fan, W. Li, Z. Zhu, Dr. H. Huang
School of Pharmaceutical Science (Shenzhen)
Shenzhen Campus of Sun Yat-sen University
Sun Yat-sen University
Shenzhen 518107 (P. R. China)
E-mail: huanghy87@mail.sysu.edu.cn

Y. Rong, S. Guo, Dr. J. Wang
School of Bioscience and Biopharmaceutics, Guangdong Province Key Laboratory for Biotechnology Drug Candidates,
Guangdong Pharmaceutical University
Guangzhou 510006 (P. R. China)

Dr. T. Sadhukhan, Dr. K. Raghavachari
Department of Chemistry
Indiana University Bloomington,
Bloomington, IN 47405 (USA)

S. Liang
PerkinElmer, Inc.
Guangzhou 510370 (P. R. China)

Z. Yuan, S. Ji
Light Industry and Chemical Engineering College
Guangdong University of Technology
Guangzhou 510006 (P. R. China)

R. Kushwaha, Dr. S. Banerjee
Department of Chemistry
Indian Institute of Technology (BHU)
Varanasi, UP 221005 (India)
E-mail: samya.chy@itbhu.ac.in

based anticancer drugs within individual cancer cells is highly important to develop efficient anticancer drug candidates.[21] Unfortunately, the traditional methodologies such as inductively coupled plasma mass spectrometry (ICP-MS) can only measure the total metal content in a cell population (assuming equal uptake efficiency of all the cells).[22] Fluorescent confocal microscopy can clearly image the localization of emissive metal complexes at the single-cell level but cannot provide any quantitative information about the cellular uptake, and only a few cells can be imaged.[23] To overcome these problems, recently, single-cell ICP-MS (SC-ICP-MS) has been developed for the rapid and quantitative analysis of the metal accumulation in individual cells rather than in a whole population of cells.[24] As this methodology has been developed very recently, the quantification of intracellular iridium contents in single cells has not been explored so far.

The two above mentioned unexplored challenges in research on metal-based catalytic cancer drugs gave us the backdrop for the present work. Herein, we report the unique application of SC-ICP-MS for the rapid and accurate quantification of iridium in single cancer cells with the photoactivable Ir^{III} complexes **Ir1** and **Ir2**. This methodology allowed us to study the intracellular uptake and retention of **Ir1** and **Ir2** at the single-cell level. The organometallic, dinuclear Ir^{III} complex **Ir2** showed excellent cell uptake efficiency and cellular retention relative to that of its mononuclear analog, **Ir1**. Moreover, **Ir2** exhibited higher photocatalytic NAD(P)H oxidation activity than **Ir1**. **Ir2** localized in the cell lysosome and showed excellently low *in vivo* dark toxicity. Interestingly, **Ir2** was highly photocytotoxic (under 525 nm light) against several cancer cell lines. The observed photoactivated anticancer activity of **Ir2** is shown to be related to its propensity for photocatalytic NAD(P)H and amino acid photo-oxidation, which in turn generated multiple ROS and carbon-centered radicals (Scheme 1).

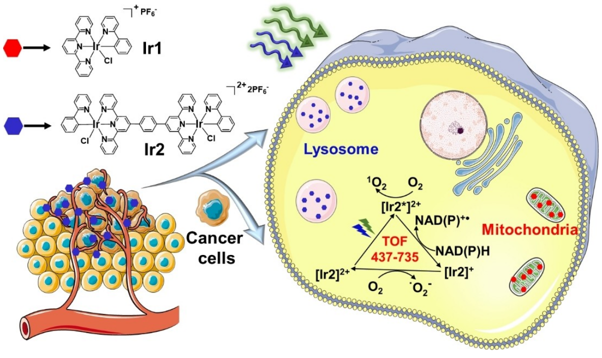

Scheme 1. Mechanism of the photo-oxidation of NAD(P)H induced by Ir^{III} photocatalysts and the subsequent generation of various reactive oxygen species.

Results and Discussion

Ir1 and **Ir2** were prepared in moderate yields as a yellow and an orange-red solid, respectively, from the reaction of 2-phenylpyridine (ppy) with the appropriate Ir^{III}-based precursors in ethylene glycol (Scheme S1). The complexes were well characterized by spectroscopic and analytical data (Figures S1–S6). Interestingly, the photophysical properties of the dinuclear complex **Ir2** showed a synergism but not an additive effect. **Ir2** exhibited a much higher absorption molar extinction coefficient than **Ir1**, especially at a longer wavelength (**Ir1** $\varepsilon_{525nm} = 115\ M^{-1}cm^{-1}$, **Ir2** $\varepsilon_{525nm} = 6129\ M^{-1}cm^{-1}$, Table S1) which was necessary to achieve high photosensitization efficient under green light (Figure 1A and Figure S7). The phosphorescence intensity of the dinuclear complex **Ir2** was about three times stronger than that of the mononuclear **Ir1** in CH_2Cl_2 (Figure 1A). The strong phosphorescence of **Ir2** was helpful to track its intracellular localization. The two complexes were stable in PBS and cell culture medium (DMEM) in the dark even up to 48 h (Figure S8) or under light exposure (465 nm and 525 nm) in PBS (Figure S9). It is important to note that the complexes exhibited greater photostability than the reference photosensitizer chlorin e6 (Ce6) (Figure S10). Interestingly, the complexes showed comparable photostability to those widely used Ir^{III} photocatalysts, such as $[Ir(ppy)_2bpy]PF_6$, $[Ir(ppy)_2dtbbpy]PF_6$ and $[Ir(dFCF_3ppy)_2bpy]PF_6$ [ppy = 2-phenylpyridine, bpy = bipyridine, dtbbpy = 4,4′-di-*tert*-butyl-2,2′-bipyridine, $dFCF_3ppy$ = 2-(2,4-difluorophenyl)-5-trifluoromethylpyridine] (Figure S10).

The excellent photo- and dark-stability of the complexes indicate that these Ir^{III} complexes can be used as stable photocatalysts as well as photosensitizers for cellular applications. Moreover, **Ir1** and **Ir2** showed polarity- (Figure S11) and viscosity-dependent phosphorescence (Figure 1B and Figure S12) in various solvents. Phosphorescence enhancement with increasing viscosity of the solution indicated the feasibility of the photosensitization process in the highly viscous intracellular environment.[25] Besides, the emission quantum yields of **Ir1** (11.3 %) and **Ir2** (3.6 %) were higher than the reference complex $[Ru(bpy)_3]Cl_2$ (2.8 %) in H_2O at room temperature (Table S1).[26] In addition, oxygen was found to significantly influence the emission intensity (Figure S13) and the excited state lifetime of **Ir1** and **Ir2** (**Ir2**: 1.57/2.48 μs, O_2/N_2) (Figure S14A and Table S1), indicating the possible excited state interaction of the Ir^{III} complexes with $^3O_2$. Such interactions in cancer cells might generate intracellular ROS which can damage the cancer cells.[27] To further explore the triplet-excited-state characteristics, the nanosecond time-resolved transient absorption (TA) of **Ir1** and **Ir2** was investigated in a nitrogen-purged CH_2Cl_2 solution. Under a 355 nm laser pulse, **Ir2** showed ground-state bleaching at 415 nm with excited-state absorption at 443 nm and 823 nm (Figure 1C), which indicated the formation of the triplet excited state (**Ir2***). The TA spectra of **Ir1** were somewhat similar to those of **Ir2** (Figure S14B). The decay of TA signals was monitored, and the triplet-excited-state lifetime of **Ir2*** (τ) at 443 nm was

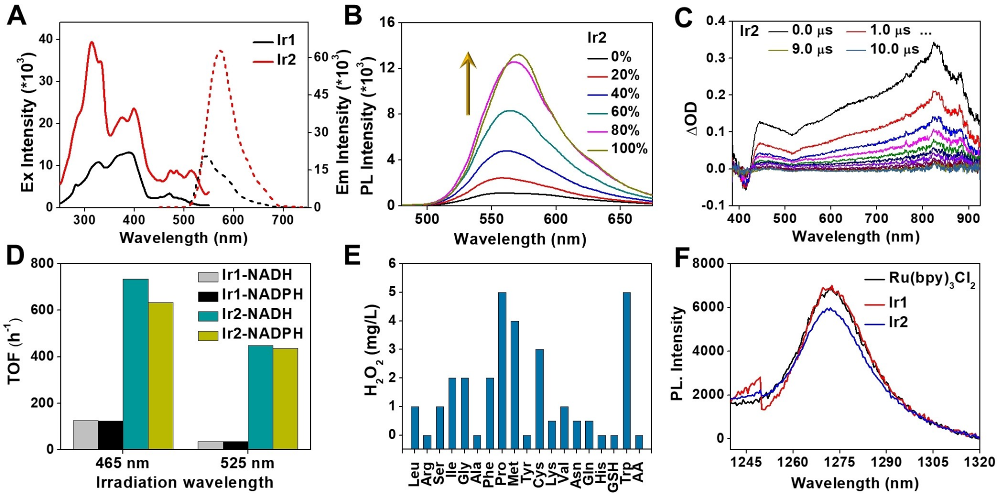

Figure 1. A) The phosphorescence excitation (solid lines) and emission (dotted lines) spectra of **Ir1** and **Ir2** (10 µM) in CH_2Cl_2 at 298 K ($\lambda_{ex}=405$ nm). B) Phosphorescence spectra of **Ir2** (10 µM) in glycerol–H_2O mixtures at 298 K (0–100 % glycerol, $\lambda_{ex}=405$ nm). C) Time-resolved transient spectra of **Ir2** (50 µM) in deaerated CH_2Cl_2 after pulsed excitation, $\lambda_{ex}=355$ nm. D) Turnover frequencies of **Ir1** and **Ir2** for NAD(P)H photo-oxidation under 465 nm (11.7 J cm^{-2}) or 525 nm (29.56 J cm^{-2}) light. E) Photocatalytic generation of H_2O_2 by **Ir2** (1 µM) in the presence of amino acids as was observed with the H_2O_2 test sticks. AA = all amino acids with **Ir2** (1 µM) in the dark for 30 min. F) Measurement of $^1O_2$ generation quantum yields of the complexes and $[Ru(bpy)_3]Cl_2$ by the direct measurement of near-infrared singlet-oxygen phosphorescence in MeOH ($\lambda_{ex}=525$ nm). All samples were isoabsorptive (A = 0.1) at 525 nm.

measured to be 3.62 µs (Figure S14C), which is 1.5 times longer than the emission lifetime ($\tau=2.48$ µs, Table S1). The long triplet-excited-state lifetime of **Ir2** might facilitate photosensitization and photo-induced electron transfer processes on light activation.

Density functional theory (DFT) calculations were carried out on the monocationic complex **Ir1** and dicationic complex **Ir2** (Figure S15). The computed redox potentials showed that the redox behaviors in the ground and excited states of the two complexes are different (Table S5). The introduction of an additional metal ion changed the ground state reduction and excited state oxidation values by ≈0.3 V, whereas the ground state oxidation and excited state reduction values changed by ≈0.2 V. At the excited state, **Ir2** ($[\mathbf{Ir2}^*]^{2+}/[\mathbf{Ir2}]^{+}=+1.42$ V) was more oxidative than **Ir1** ($[\mathbf{Ir1}^*]^{+}/[\mathbf{Ir1}]^{0}=+1.22$ V). Taking the high molar extinction coefficient, microsecond level excited-state lifetime, and high excited-state redox potential into consideration, **Ir2** has the potential to be an excellent photocatalyst.

In recent years, NAD(P)H has become a hot target for cancer drug development due to its key roles in many important cellular processes such as in ATP production, the mitochondrial electron transport chain (ETC), and the synthesis of biomolecules.[28] Depletion of intracellular NAD(P)H is reported to cause cancer cell death.[29] As our complexes have significantly long triplet-excited-state lifetimes and high excited-state redox potentials, we explored the potential of the complexes as photoredox catalysts for NAD(P)H oxidation.[3,15] **Ir2**, remarkably, turned out to be a highly potent photocatalyst for NAD(P)H oxidation with very high turnover frequencies (TOFs) (Figure S16). It is important to discuss that the TOFs of **Ir2** (ca. 735 h^{-1} at 465 nm and ca. 448 h^{-1} at 525 nm, Figure 1D and Table S2) for NADH photo-oxidation are much higher (4.5–7.3 times) than those given in some earlier reports.[3,15] This could be due to the presence of two active sites (Ir^{III}) in **Ir2**, evident from the observation that TOFs of the analogous mononuclear complex (**Ir1**) were around 6–13 times lower than that of **Ir2** (Figure 1D and Table S2). The finding that **Ir2** also induced NADH photo-oxidation at 525 nm is important, considering the fact that nowadays, green light photosensitizers are attracting interest to treat skin and bladder cancers as the penetration depth of green light matches the thickness of the skin or bladder tumors.[30] Moreover, **Ir2** also exhibited photo-oxidation of amino acids such as proline and tryptophane, along with H_2O_2 generation (Figure 1E). It is important to note here that currently we can only envision that during light irradiation, the excited state **Ir2*** extracts an electron from the N atom of amino acid (similar to electron extraction from NAD(P)H). After this step, probably the strongly reductive **Ir2$^{(II)}$** interacts with oxygen to generate H_2O_2, which was detected by H_2O_2 test paper. The exact mechanism and final oxidized products are not very clear at this moment. Interestingly, when present alone in solution, **Ir2** generated a significant amount of singlet oxygen ($^1O_2$) upon 465 and 525 nm light irradiation, as was detected using 9,10-anthracenediyl-bis(methylene) dimalonic acid (ABDA) as the $^1O_2$ probe (Figure S17).[31] The singlet oxygen quantum yield (Φ_Δ) of the complexes was determined by the direct measurement of near-IR singlet oxygen phosphorescence (Figure 1F). It was found that Φ_Δ of **Ir1** (0.82) is slightly higher than that of **Ir2** (0.75). This data indicates that the presence of the two Ir^{III} centers in **Ir2** does not affect the $^1O_2$ production significantly and the complexes at the excited state interact efficiently with the $^3O_2$ to produce $^1O_2$. All these observations clearly indicate that **Ir2** has the potential to act as a multitargeting and multifunctional anticancer agent, as it can act like a typical type II photosensitizer as well as a type I photocatalyst.

The remarkable NAD(P)H photo-oxidation and photo-induced ROS generation abilities of **Ir2** promoted us to study its photo-activated anticancer profile *in vitro* and *in vivo*. The intracellular uptake, localization, and retention of drug molecules are directly related to the drug efficacy and mechanism of drug action.[32] Thus, the measurement of Ir content in individual cancer cells could serve as a primary marker of the anticancer efficiency of the complexes. It is important to mention that the conventional method to determine intracellular metal uptake includes steps like 1) isolation of cells, 2) digestion of cells, and 3) measureement of metal content. This methodology suffers from limitations such as 1) the significant long time required for the whole procedure and 2) the assumption that all cells will take up metal complex equally.[33]

SC-ICP-MS (Figure 2A) is emerging as a very fast and accurate method to determine element content within individual cells.[34] We took the advantage of this method to compare the time-dependent intracellular uptake and retention of **Ir1** and **Ir2** in HepG2 cancer cells. As the incubation time extended, the number and intensity of Ir spike signal events (Figure 2B) and Ir content per single cell (Figure 2C) of **Ir2** within cells were more than two times higher than with **Ir1**, possibly due to the highlipophilicity of **Ir2** that promoted cellular uptake process(log P **Ir1**/**Ir2**, 0.13/0.54). Besides, the intracellular amount of **Ir2** ranged from 20 and up to 400 ag per cell, indicating that the cellular uptake of **Ir2** differed within the cell population. In this way, SC-ICP-MS provides more detailed cell uptake information than that obtained by conventional ICP-MS, which used bulk analysis (Figure S18).

Furthermore, the intracellular retention of **Ir1** and **Ir2** was investigated by SC-ICP-MS as well. For this study, cells were cleaned with PBS to remove the excess **Ir2** after 12 h of incubation with **Ir2**, and then the intracellular Ir content was analyzed after 8 h. As shown in Figure 2D, the individual cellular Ir content was found to be almost the same even 8 h after drug removal, indicating very high retention ability of **Ir2** in HepG2 cells. However, under the same conditions, the cellular content of **Ir1** decreased significantly (Figure 2D). Overall, the SC-ICP-MS studies demonstrate the efficient intracellular uptake and thereafter significantly high retention of **Ir2** in cancer cells. Moreover, as the high efflux of cisplatin was reported to be one of the major reasons for drug resistance,[35] the high intracellular retention of **Ir2** is expected to be useful to overcome the drug resistance problem.

We further investigated the cellular localization of **Ir2** in cancer cells by confocal laser scanning microscopy with various organelle trackers. As shown in Figure 3A, the green intracellular emission of **Ir2** significantly merged with the red fluorescence of Lyso-Tracker Red, clearly showing that **Ir2** mainly localized in the lysosomes. For comparison, the mononuclear complex, **Ir1**, was mainly located in both mitochondria and lysosomes (Figure S19). It is worthy to mention thatthe lysosome has emerged as the new target for cancer phototherapy recently, as lysosomal localization is reported to effectively reduce the dark cytotoxicity and can thus enhance the therapeutic effect of cancer phototherapy.[36] In contrast, mitochondria-targeting photosensitizers may exhibit dark toxicity sometimes as this organelle plays an important role in programmed cell death.[37]

The excellent intracellular uptake and retention of the complexes are important factors in this study as **Ir1** and **Ir2**

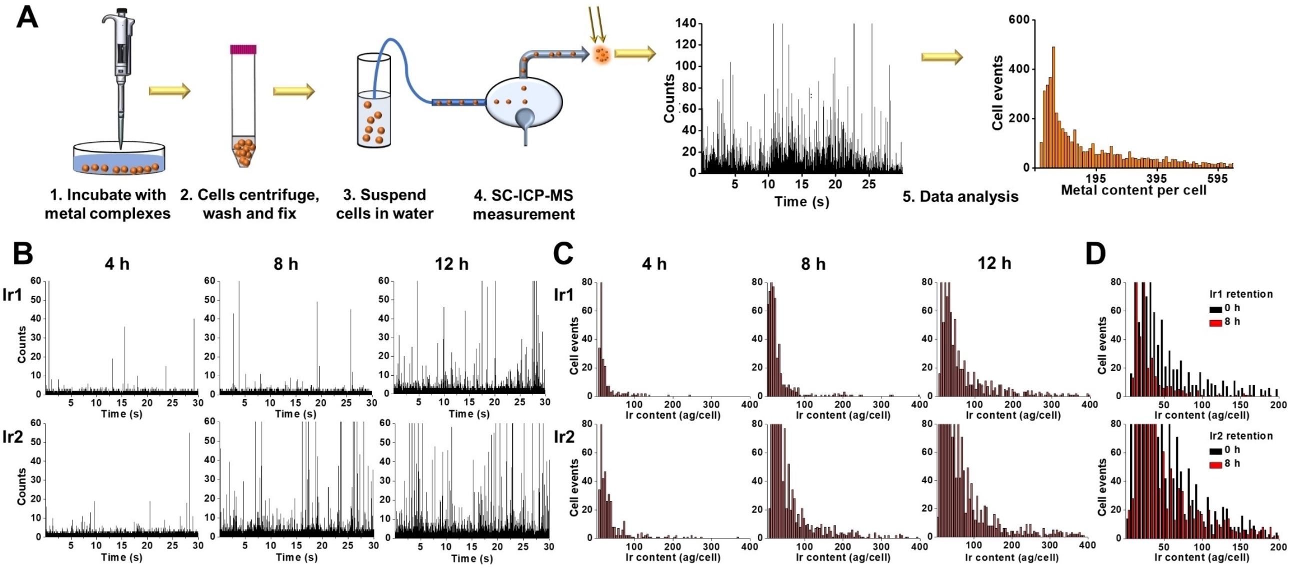

Figure 2. Estimation of the intracellular amount of Ir^{III} photoredox catalysts by SC-ICP-MS. A) Schematic illustration of the SC-ICP-MS procedure. B) SC-ICP-MS results showing the time-dependent uptake of **Ir1** and **Ir2** (10 μM) in individual cancer cells. C) SC-ICP-MS histograms showing the iridium uptake in individual cancer cells when incubated with **Ir1** and **Ir2** (10 μM). D) Mass histograms showing the intracellular iridium retention after removal of **Ir1**- and **Ir2**-containing medium.

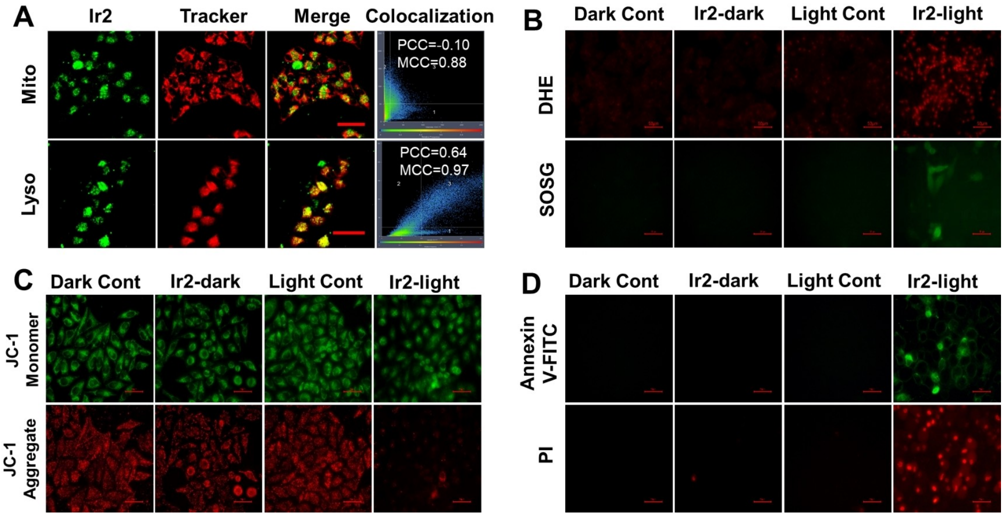

Figure 3. A) In-cell localization of **Ir2** (10 μM) in HepG2 cells, co-stained with Mito-tracker and Lyso-tracker dyes. $\lambda_{ex}/\lambda_{em}$: 405/580 nm for **Ir2** and 633/680 nm for Mito-tracker and Lyso-tracker. Pearson's correlation coefficient (PCC) and Manders' colocalization coefficient (MCC) are also provided. Scale bar: 50 μm. B) $O_2^{\bullet-}$ and $^1O_2$ generation by **Ir2** as determined by DHE (5 μM) and SOSG (10 μM) in HepG2 cells with or without irradiation at 525 nm (29.56 J cm^{-2}). Scale bar: 50 μm. C) JC-1 staining images of HepG2 cells treated with **Ir2** (10 μM) and with or without irradiation at 525 nm (29.56 J cm^{-2}). Scale bar: 50 μm. D) Annexin V-FITC/PI dual staining images of cancer cells treated with **Ir2** (10 μM) either with or without irradiation at 525 nm (29.56 J cm^{-2}). Scale bar: 50 μm.

can induce ROS generation and NAD(P)H oxidation upon light exposure to kill cancer cells. Interestingly, **Ir2** did not show significant dark toxicity (IC_{50} = 48–200 μM) against a normal cell line NP69 (nasopharynx) or the cancer cell lines HepG2 (liver), A549 (lung), A549/DDP (cisplatin-resistant lung), and HeLa (cervix). **Ir2** became highly toxic (IC_{50} = 0.3–4.1 μM, Table S3) toward cancer cells upon photo-irradiation with 525 nm light (29.56 J cm^{-2}). Thus, **Ir2** is not harmful to the cells without light irradiation. The best photo-activation anticancer effect of **Ir2** was achieved against HepG2 cells, where the photo-therapeutic index (PI = Dark IC_{50}/Light IC_{50}) on 525 nm light irradiation was ca. 660. To the best of our knowledge, such a high PI value with Ir^{III} based photosensitizers is very rare.[5–14] It is important to note that the highest PI values reported with Ir^{III} based photosensitizers are in the range of 8–250 (Table S6).[5–14] Thus, the PI value of **Ir2** (ca. 660 in HepG2 cells) is much higher than that of the other reported Ir^{III}-based photosensitizers.[5–14] Moreover, PI values of **Ir2** against A549 and A549/DDP cancer cells were ca. 36 and 80 respectively, again higher than for complexes reported in refs. [5–14]. Here it's worthy to mention that **Ir2** was highly anticancer active against the cisplatin-resistant A549/DDP cells with a PI value of ca. 80. Thus, this complex has the potential to overcome the drug resistance problem of cisplatin. In comparison to **Ir2**, the photo-cytotoxicity of **Ir1** was significantly reduced, probably due to its low in-cell accumulation, low light absorption ability, low levels of cellular ROS generation, and low NAD(P)H oxidation efficiency. Remarkably, **Ir2** exhibited a much higher photo-cytotoxicity and photo-therapeutic index than the clinical PDT prodrug 5-aminolevulinic acid (5-ALA) under identical experimental conditions. Considering the fact that in PDT/photo-chemotherapy, only the tumor region is irradiated and **Ir2** is not toxic against normal cells, this complex may have minimal side effects during PDT. Under hypoxia (5 % O_2) in HepG2 cells, the dark and photo (525 nm, 29.56 J cm^{-2}) IC_{50} of **Ir1** were all above 200 μM, indicating that **Ir1** was not toxic at all under hypoxia, which was in line with its extremely low light absorption ability at 525 nm. In the case of **Ir2**, the dark and photo (525 nm, 29.56 J cm^{-2}) IC_{50} were measured to be 90.2 μM and 25.7 μM, respectively, with photo index ca. 3.5. Thus, the photo-cytotoxic potential of **Ir2** reduced under hypoxia, indicating that molecular O_2 plays an important role for the anticancer mechanism of **Ir2** (Scheme 1).

The observed photo-activated anticancer activity of **Ir2** was closely related to its propensity for in-cell ROS formation, as was evident from the 2′,7′-dichlorodihydrofluorescein diacetate (DCFH-DA) assay.[38] In irradiated cancer cells, **Ir2** generated intracellular ROS that oxidized intracellular DCFH (formed by intracellular esterase catalyzed DCFH-DA hydrolysis) to the strong green fluorescent DCF (Figure S20). Interestingly, the total photo-induced intracellular ROS generated by **Ir2** was a mixture of superoxide radical and $^1O_2$, as was proved by with the superoxide probe dihydroethidium (DHE)[39] and the $^1O_2$ probe singlet oxygen sensor green (SOSG),[40] respectively (Figure 3B). It is important to note that **Ir2** did not generate any significant ROS in the dark. As a result of photo-induced intracellular ROS generation and NAD(P)H photo-oxidation, **Ir2** induced a significant change in the mitochondrial membrane potential (MMP) only after light irradiation (525 nm, 29.56 J cm^{-2}) in HepG2 cells (Figure 3C). Interestingly, **Ir1** did not change the MMP even after light exposure. This result could be due to the relatively slow and low cellular uptake ability of **Ir1** (confirmed by SC-ICP-MS data). Moreover, the low molar extinction coefficient of **Ir1** at

525 nm also contributed to the resultant low photocytotoxicity of **Ir1**. To gain insight into **Ir2**-induced change in MMP upon photo-irradiation, we investigated the cellular localization of **Ir2** after the light irradiation. However, it was found that **Ir2** did not transfer to the mitochondria after light irradiation (Figure S21). We further incubated HepG2 cells with the mitochondria-targeting superoxide probe MitoSOX[41] and found that the superoxide signal in mitochondria indeed increased significantly after light irradiation in the presence of **Ir2** (Figure S22). **Ir1** was less active in generating superoxide anions in mitochondria (Figure S22) and thus could not change the MMP efficiently (Figure S23). Taking the cellular localization and superoxide experiment (DHE experiment) into consideration (Figure 3B), we may envision that the photo-generated superoxide by **Ir2** is transferred from the lysosome to the mitochondria during irradiation and ultimately causes the MMP change. Moreover, as the result of photo-induced intracellular ROS generation, NAD(P)H oxidation and MMP alteration, **Ir2** induced necro-apoptotic cell death, which was evident from the Annexin V-FITC/PI dual staining assay (Figure 3D).[42] Although the exact mechanism of cell death requires further in-depth investigation, it is important to mention that Lin et al. previously found that necro-apoptotic cell deathwas correlated with the development of anticancer immune response.[43]

The highly promising in vitro anticancer activity of **Ir2** promoted us to explore its *in vivo* biocompatibility and cancer photo-therapeutic activity. We evaluated the biocompatibility of **Ir2** in the dark with green fluorescent protein transfectedFLK zebrafish (*Tg(flk1:EGFP)^{s843}*).[44] The biocompatibility of **Ir2** was evaluated by morphological observations (e.g., heart rate monitoring, tail contraction, etc.) of the GFP fluorescence type zebrafish model. As shown in Figure S24A,the body morphological indicators such as body shape, bones and organs of zebrafish treated with **Ir2** were consistent with the untreated control, indicating excellent *in vivo* biocompatibility of **Ir2**. Moreover, the normal heart rate and swimming behavior also supported the excellent biocompatibility of **Ir2** in the zebrafish model. Furthermore, we also evaluated the maximum tolerated dose (MTD) of **Ir2** in mice according to the metric of MTD by intraperitoneal injection (IP). The mice were randomly divided into five groups ($n=5$ per group) and treated with 0, 5, 10, 20, 30 mg kg^{-1} of **Ir2** in the dark, respectively. As shown in Figure S24B, the bodyweight gains of mice treated with **Ir2**, especially with the highest dose of 30 mg kg^{-1}, showed no significant difference from the 0 mg kg^{-1} group during the 27 days of the experiment. Moreover, the H&E staining of the vital organs of mice indicated that the 30 mg kg^{-1} dose of **Ir2** was not toxic in the dark (Figure S24C).

The excellent *in vitro* photo-toxicity and *in vivo* biocompatibility of **Ir2** inspired us to investigate the phototoxicity profile of **Ir2** *in vivo* against the HepG2 tumor-bearing mouse model. Seven days after HepG2 cells was injected into mice, the mice were randomly distributed into four groups ($n=5$): Control group, only light group, only **Ir2** (without light) group, and **Ir2**+light group. **Ir2** was injected intratumorally at a dose of 1.0 mg kg^{-1}. The **Ir2**+light group was irradiated by 525 nm light (88.68 J cm^{-2}) 60 min after **Ir2** injection. Tumor volumes were measured every two days to note the therapeutic effect (if any). As shown in Figure 4A, the tumor volume of the control group, only light, or only **Ir2** group was found to increase significantly from 8–14 days. In contrast, tumor growth in the **Ir2**+light group was remarkably low. The tumors were removed and then weighed. The tumor weight in the **Ir2**+light group was much lower than that of the other groups (Figure 4B,C). There was very little difference in the body weights and H&E staining profiles of major organs between the four groups (Figure 4D and Figure S25), revealing that **Ir2** can effectively inhibit tumor growth upon 525 nm light irradiation without harming the normal body growth of mice. H&E and TUNEL staining assays of tumor sections were performed to investigate the therapeutic effect by histological analysis. As shown in Figure 4E, the H&E and TUNEL staining of the tumor section of **Ir2**+light showed significant apoptosis and necrosis, confirming the *in vivo* therapeutic effect of **Ir2** upon 525 nm light irradiation.

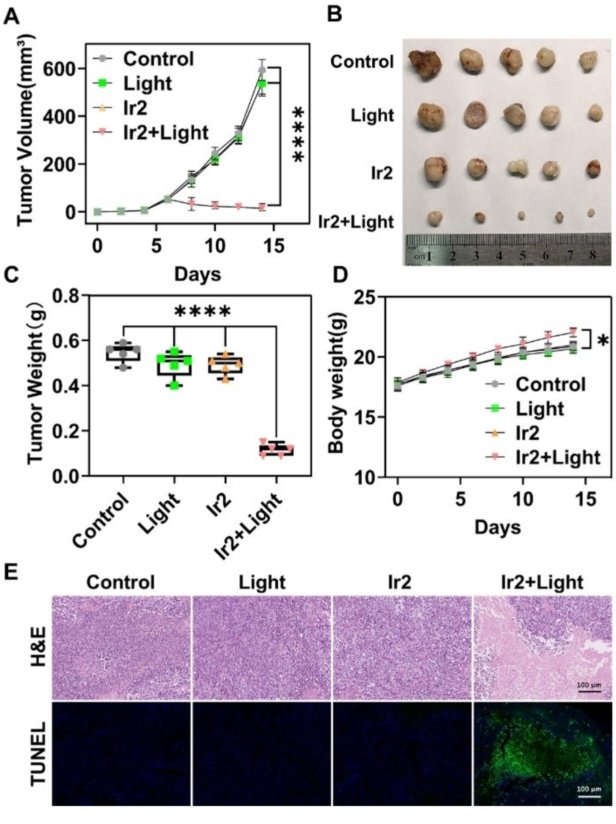

Figure 4. *In vivo* photo-therapeutic activity of **Ir2** against HepG2 mice model. A) Tumor growth curves of mice after injection with HepG2 cells. On day 7, mice were given various treatments. B) Pictures of tumors collected from mice of different groups on the seventh day after various treatments. C) Averaged weights of tumors shown in (B) (****$p<0.0001$, ***$p<0.0002$, **$p<0.0021$, or *$p<0.0332$). D) Averaged body weights of four groups of mice. E) H&E staining images and TUNEL assay images of tumor tissue of mice after various treatments. Scale bar: 100 μm.

Conclusion

In conclusion, we reported here a novel photo-stable and phosphorescent organometallic dinuclear Ir^{III} complex (**Ir2**) as both excellent photosensitizer and efficient photocatalyst for NAD(P)H and amino acid oxidation. The NAD(P)H photocatalytic activity of **Ir2** was 13 times higher than that of the mononuclear complex **Ir1**, indicating a significant synergism but not an additive effect. Thus, the photocatalytic activity of this type of Ir^{III} complex can be tuned by increasing the number of metal ions. **Ir2**, which was lysosome-targeting and highly biocompatible, exhibited remarkably high photo-activated anticancer activity against several types of cancer cell lines in vitro and a HepG2 tumor-bearing mice model *in vivo.* The photo-activated anticancer activity of **Ir2** was due to the ability of photocatalytic oxidation of NAD(P)H and amino acid. Oxidation of NAD(P)H and amino acids resulted in multiple ROS generation that also contributed toward the resultant anticancer activity. Thus **Ir2** has the potential to act as a multifunctional anticancer agent. The photo-cytotoxicity of **Ir2** at 525 nm was significantly higher (5–80 times depending on cell lines) than that of **Ir1**, probably due to the higher intracellular ROS generation and NAD(P)H oxidation ability of **Ir2** and the lack of absorbance of **Ir1** at 525 nm, as was evident from the in-solution and *in vitro* studies. We also took the advantage of single-cell inductively coupled plasma mass spectrometry (SC-ICP-MS) to accurately quantify the amount of iridium taken up by the individual cells. It is important to note that this is the very first report where SC-ICP-MS is used to quantify Ir complexes at the single-cell level. Furthermore, it is worthy to mention that we have reported the in-cell photocatalytic anticancer profile of a dinuclear metallic photo-redox catalyst for the first time in this work.

Acknowledgements

We acknowledge the financial support from the National Natural Science Foundation of China (NSFC 22007104, 21771042, 21975053); Guangdong Basic and Applied Basic Research Foundation (2019A1515110601, 2021B1515020050); Science, Technology and Innovation Commission of Shenzhen Municipality Project (JCYJ20190807152616996); the "Summit Plan" High-level hospital construction project of Foshan (FSSYKF-2020002); DST, Government of India (DST/INSPIRE/04/2019/000492); and the U.S. National Science Foundation (CHE-1764264).

Conflict of Interest

The authors declare no conflict of interest.

Data Availability Statement

Research data are not shared.

Keywords: Antitumor agents · Iridium Complexes · Photocatalysis · Photodynamic Therapy · Single-Cell ICP-MS

[1] F. Bray, M. Laversanne, E. Weiderpass, I. Soerjomataram, *Cancer* **2021**, *127*, 3029–3030.

[2] a) S. Banerjee, P. J. Sadler, *RSC Chem. Biol.* **2021**, *2*, 12–29; b) F. Heinemann, J. Karges, G. Gasser, *Acc. Chem. Res.* **2017**, *50*, 2727–2736; c) Z. Fan, J. Huang, H. Huang, S. Banerjee, *ChemMedChem* **2021**, *16*, 2480–2486.

[3] C. Huang, C. Liang, T. Sadhukhan, S. Banerjee, Z. Fan, T. Li, Z. Zhu, P. Zhang, K. Raghavachari, H. Huang, *Angew. Chem. Int. Ed.* **2021**, *60*, 9474–9479; *Angew. Chem.* **2021**, *133*, 9560–9565.

[4] a) X. Zhao, J. Liu, J. Fan, H. Chao, X. Peng, *Chem. Soc. Rev.* **2021**, *50*, 4185–4219; b) C. Imberti, P. Zhang, H. Huang, P. J. Sadler, *Angew. Chem. Int. Ed.* **2020**, *59*, 61–73; *Angew. Chem.* **2020**, *132*, 61–73.

[5] a) L. Guo, H. Zhang, M. Tian, Z. Tian, Y. Xu, Y. Yang, H. Peng, P. Liu, Z. Liu, *New J. Chem.* **2018**, *42*, 16183–16192; b) C. Wang, J. Liu, Z. Tian, M. Tian, L. Tian, W. Zhao, Z. Liu, *Dalton Trans.* **2017**, *46*, 6870–6883; c) D. Kong, L. Guo, M. Tian, S. Zhang, Z. Tian, H. Yang, Y. Tian, Z. Liu, *Appl. Organomet. Chem.* **2019**, *33*, e4633; d) J. Li, M. Tian, Z. Tian, S. Zhang, C. Yan, C. Shao, Z. Liu, *Inorg. Chem.* **2018**, *57*, 1705–1716.

[6] B. Liu, S. Monro, L. Lystrom, C. G. Cameron, K. Colo, H. Yin, S. Kilina, S. A. McFarland, W. Sun, *Inorg. Chem.* **2018**, *57*, 9859–9872.

[7] K. Xiong, Y. Zhou, X. Lin, J. Kou, M. Lin, R. Guan, Y. Chen, L. Ji, H. Chao, *Photochem. Photobiol.* **2022**, *98*, 85–91.

[8] R. Bevernaegie, B. Doix, E. Bastien, A. Diman, A. Decottignies, O. Feron, B. Elias, *J. Am. Chem. Soc.* **2019**, *141*, 18486–18491.

[9] A. M.-H. Yip, C. K.-H. Lai, K. S.-M. Yiu, K. K.-W. Lo, *Angew. Chem. Int. Ed.* **2022**, *61*, e202116078; *Angew. Chem.* **2022**, *134*, e202116078.

[10] S. Yi, Z. Lu, J. Zhang, J. Wang, Z. Xie, L. Hou, *ACS Appl. Mater. Interfaces* **2019**, *11*, 15276–15289.

[11] C. Lu, W. Xu, H. Shah, B. Liu, W. Xu, L. Sun, S. Y. Qian, W. Sun, *ACS Appl. Bio Mater.* **2020**, *3*, 6865–6875.

[12] M. Shao, M. Yao, X. Liu, C. Gao, W. Liu, J. Guo, J. Zong, X. Sun, Z. Liu, *Inorg. Chem.* **2021**, *60*, 17063–17073.

[13] V. Novohradsky, A. Rovira, C. Hally, A. Galindo, G. Vigueras, A. Gandioso, M. Svitelova, R. B. Obach, H. Kostrhunova, L. Markova, J. Kasparkova, S. Nonell, J. Ruiz, V. Brabec, V. Marchan, *Angew. Chem. Int. Ed.* **2019**, *58*, 6311–6315; *Angew. Chem.* **2019**, *131*, 6377–6381.

[14] a) H. Yuan, Z. Han, Y. Chen, F. Qi, H. Fang, Z. Guo, S. Zhang, W. He, *Angew. Chem. Int. Ed.* **2021**, *60*, 8174–8181; *Angew. Chem.* **2021**, *133*, 8255–8262; b) C. Wang, L. Lystrom, H. Yin, M. Hetu, S. Kilina, S. A. McFarland, W. Sun, *Dalton Trans.* **2016**, *45*, 16366–16378; c) L. Qiao, J. Liu, S. Kuang, X. Liao, J. Kou, L. Jia, H. Chao, *Dalton Trans.* **2021**, *50*, 14332–14341.

[15] a) W. Wang, K. Vellaisamy, G. Li, C. Wu, C.-N. Ko, C.-H. Leung, D.-L. Ma, *Anal. Chem.* **2017**, *89*, 11679–11684; b) M. Wang, W. Wang, T.-S. Kang, C.-H. Leung, D.-L. Ma, *Anal. Chem.* **2016**, *88*, 981–987; c) W. Wang, T.-L. Yung, S.-S. Cheng, F. Chen, J.-B. Liu, C.-H. Leung, D.-L. Ma, *Sens. Actuators B* **2020**, *321*, 128486.

[16] H. Huang, S. Banerjee, K. Qiu, P. Zhang, O. Blacque, T. Malcomson, M. J. Paterson, G. J. Clarkson, M. Staniforth, V. G. Stavros, G. Gasser, H. Chao, P. J. Sadler, *Nat. Chem.* **2019**, *11*, 1041–1048.

[17] a) X. Li, N. Kwon, T. Guo, Z. Liu, J. Yoon, *Angew. Chem. Int. Ed.* **2018**, *57*, 11522–11531; *Angew. Chem.* **2018**, *130*, 11694–11704; b) M. A. Rajora, J. W. H. Lou, G. Zheng, *Chem. Soc. Rev.* **2017**, *46*, 6433–6469; c) W. Fan, P. Huang, X. Chen, *Chem. Soc. Rev.* **2016**, *45*, 6488–6519.

[18] a) G. Li, D. Zhu, X. Wang, Z. Su, M. R. Bryce, *Chem. Soc. Rev.* **2020**, *49*, 765–838; b) L. Zhang, Y. Li, W. Che, D. Zhu, G. Li, Z. Xie, N. Song, S. Liu, B. Z. Tang, X. Liu, Z. Su, M. R. Bryce, *Adv. Sci.* **2019**, *6*, 1802050.

[19] A. Krishan, C. M. Fitz, I. Andritsch, *Cytometry* **1997**, *29*, 279–285.

[20] L. Galluzzi, L. Senovilla, I. Vitale, J. Michels, I. Martins, O. Kepp, M. Castedo, G. Kroemer, *Oncogene* **2012**, *31*, 1869–1883.

[21] a) D. Clases, M. Sperling, U. Karst, *TrAC Trends Anal. Chem.* **2018**, *104*, 135–147; b) S. Theiner, A. Schoeberl, A. Schweikert, B. K. Keppler, G. Koellensperger, *Curr. Opin. Chem. Biol.* **2021**, *61*, 123–134.

[22] a) A. R. Timerbaev, *J. Anal. At. Spectrom.* **2021**, *36*, 254–266; b) R. N. Rao, M. K. Talluri, *J. Pharm. Biomed. Anal.* **2007**, *43*, 1476–1482.

[23] a) X. Huang, J. Song, B. C. Yung, X. Huang, Y. Xiong, X. Chen, *Chem. Soc. Rev.* **2018**, *47*, 2873–2920; b) M. Mauro, A. Aliprandi, D. Septiadi, N. S. Kehr, L. De Cola, *Chem. Soc. Rev.* **2014**, *43*, 4144–4166; c) Q. Zhao, C. Huang, F. Li, *Chem. Soc. Rev.* **2011**, *40*, 2508–2524.

[24] X. Yu, M. He, B. Chen, B. Hu, *Anal. Chim. Acta* **2020**, *1137*, 191–207.

[25] a) H. Zhu, J. Fan, J. Du, X. Peng, *Acc. Chem. Res.* **2016**, *49*, 2115–2126; b) X. Yang, B. Xu, L. Shen, R. Sun, Y. Xu, Y. Song, J. Ge, *Anal. Chem.* **2020**, *92*, 3517–3521.

[26] H. Huang, B. Yu, P. Zhang, J. Huang, Y. Chen, G. Gasser, L. Ji, H. Chao, *Angew. Chem. Int. Ed.* **2015**, *54*, 14049–14052; *Angew. Chem.* **2015**, *127*, 14255–14258.

[27] S. Kwiatkowski, B. Knap, D. Przystupski, J. Saczko, E. Kędzierska, K. Knap-Czop, J. Kotlińska, O. Michel, K. Kotowski, J. Kulbacka, *Biomed. Pharmacother.* **2018**, *106*, 1098–1107.

[28] J. Zhu, S. Schwörer, M. Berisa, Y. J. Kyung, K. W. Ryu, J. Yi, X. Jiang, J. R. Cross, C. B. Thompson, *Science* **2021**, *372*, 968–972.

[29] a) J. J. Soldevila-Barreda, I. Romero-Canelo′n, A. Habtemariam, P. J. Sadler, *Nat. Commun.* **2015**, *6*, 6582; b) J. P. C. Coverdale, I. Romero-Canelo′n, C. Sanchez-Cano, G. J. Clarkson, A. Habtemariam, M. Wills, P. J. Sadler, *Nat. Chem.* **2018**, *10*, 347–354.

[30] X. Q. Zhou, M. Xiao, V. Ramu, J. Hilgendorf, X. Li, P. Papadopoulou, M. A. Siegler, A. Kros, W. Sun, S. Bonnet, *J. Am. Chem. Soc.* **2020**, *142*, 10383–10399.

[31] T. Entradas, S. Waldron, M. Volk, *J. Photochem. Photobiol. B* **2020**, *204*, 111787.

[32] X. Cao, J. Hou, Q. An, Y. Assaraf, X. Wang, *Drug Resist. Updates* **2020**, *49*, 100671.

[33] D. Beauchemin, *Anal. Chem.* **2010**, *82*, 4786–4810.

[34] L. Yin, Z. Zhang, Y. Liu, Y. Gao, J. Gu, *Analyst* **2019**, *144*, 824–845.

[35] L. Gao, Z. Wu, Y. G. Assaraf, Z. Chen, L. Wang, *Drug Resist. Updates* **2021**, *57*, 100770.

[36] Z. Zhou, J. Liu, J. Huang, T. W. Rees, H. Wang, X. Li, H. Chao, P. J. Stang, *Proc. Natl. Acad. Sci. USA* **2019**, *116*, 20296–20302.

[37] F. J. Bock, W. G. Stephen, *Nat. Rev. Mol. Cell Biol.* **2020**, *21*, 85–100.

[38] Y. He, D. Häder, *Photochem. Photobiol. Sci.* **2002**, *1*, 729–736.

[39] M. Li, Y. Shao, J. H. Kim, Z. Pu, X. Zhao, H. Huang, T. Xiong, Y. Kang, G. Li, K. Shao, J. Fan, J. W. Foley, J. S. Kim, X. Peng, *J. Am. Chem. Soc.* **2020**, *142*, 5380–5388.

[40] M. Li, J. Xia, R. Tian, J. Wang, J. Fan, J. Du, S. Long, X. Song, J. W. Foley, X. Peng, *J. Am. Chem. Soc.* **2018**, *140*, 14851–14859.

[41] H. Huang, P. Zhang, B. Yu, Y. Chen, J. Wang, L. Ji, H. Chao, *J. Med. Chem.* **2014**, *57*, 8971–8983.

[42] Z. Feng, P. Tao, L. Zou, P. Gao, Y. Liu, X. Liu, H. Wang, S. Liu, Q. Dong, J. Li, B. Xu, W. Huang, W. Wong, Q. Zhao, *ACS Appl. Mater. Interfaces* **2017**, *9*, 28319–28330.

[43] K. Lu, C. He, W. Lin, *J. Am. Chem. Soc.* **2015**, *137*, 7600–7603.

[44] S. Jin, D. Beis, T. Mitchel, J. Chen, D. Y. R. Stainier, *Development* **2005**, *132*, 5199–5209.

Manuscript received: February 8, 2022
Accepted manuscript online: March 8, 2022
Version of record online: April 6, 2022